



PERGAMON

Acta mater. 48 (2000) 2277–2295



www.elsevier.com/locate/actamat

DISCRETE AND CONTINUOUS DEFORMATION DURING NANOINDENTATION OF THIN FILMS

A. GOULDSTONE, H.-J. KOH[†], K.-Y. ZENG[‡], A. E. GIANNAKOPOULOS and
S. SURESH[§]

Department of Materials Science and Engineering, Massachusetts Institute of Technology, Cambridge,
MA 02139, USA

(Received 24 November 1999; accepted 4 January 2000)

Abstract—This paper describes nanoindentation experiments on thin films of polycrystalline Al of known texture and different thicknesses, and of single crystal Al of different crystallographic orientations. Both single-crystalline and polycrystalline films, 400–1000 nm in thickness, are found to exhibit multiple bursts of indenter penetration displacement, h , at approximately constant indentation loads, P . Recent results from the nanoindentation studies of Suresh *et al.* (Suresh, S., Nieh T.-G. and Choi, B.W., *Scripta mater.*, 1999, **41**, 951) along with new microscopy observations of thin films of polycrystalline Cu on Si substrates are also examined in an attempt to extract some general trends on the discrete and continuous deformation processes. The onset of the first displacement burst, which is essentially independent of film thickness, appears to occur when the computed maximum shear stress at the indenter tip approaches the theoretical shear strength of the metal films for all the cases examined. It is reasoned that these displacement bursts are triggered by the nucleation of dislocations in the thin films. A simple model to estimate the size of the prismatic dislocation loops is presented along with observations of deformation using transmission electron microscopy and atomic force microscopy. It is demonstrated that the response of the nanoindented film is composed of purely elastic behavior with intermittent microplasticity. The overall plastic response of the metal films, as determined from nanoindentation, is shown to scale with film thickness, in qualitative agreement with the trends seen in wafer curvature or X-ray diffraction measurements. © 2000 Acta Metallurgica Inc. Published by Elsevier Science Ltd. All rights reserved.

Keywords: Mechanical properties; Nanoindentation; Thin films; Theory and experiments; Dislocations

1. INTRODUCTION

Advances in testing methods have led to the general availability of instrumented micro- and nanoindenters. Nanoindenters provide accurate measurements of the continuous variation of indentation load, P , down to levels of micro-Newtons, as a function of the indenter penetration depth, h , down to levels of nanometers. Numerous investigations of instrumented indentation have been performed on a variety of material systems, with the objective of extracting mechanical properties and/or residual stresses (e.g. [1–5]). Parallel efforts have been undertaken to develop comprehensive theoretical and computational models, in an attempt to elucidate the

mechanics and mechanisms of indentation and to characterize the mechanical properties (e.g. [2–9]).

The indentation of metallic materials has been a topic of considerable complexity due to such factors as the indenter size, shape and tip geometry, and the material strain hardening characteristics (which influence the pile-up or sink-in of the material around the indenter and which cannot be experimentally assessed *in situ* during instrumented indentation). Despite these issues, there is a growing body of experimental and theoretical information which reveals that, in addition to providing a useful tool for the characterization of local properties and internal stresses in materials, instrumented indentation can also offer insights into microscopic deformation processes such as defect nucleation. For example, nanoindentation of bulk Au, W and Fe–Si crystals has shown that defect nucleation could possibly be associated with the onset of abrupt bursts in indenter penetration distance into the material (e.g. [10–17]). A careful analysis of such phenomena, particularly for the case of thin films

[†] Present address: Samsung Display Devices Co., CRT Development Team, SDI 575 Shin-dong, Paldal-gu, Suwon, Kungki-do 442-391, S. Korea.

[‡] Present address: Institute of Materials Research and Engineering, 3 Research Link, Singapore 117602.

[§] To whom all correspondence should be addressed.

on substrates, could potentially offer insights into the size-dependence of elastoplastic deformation and mechanisms of microplasticity.

Nanoindentation of thin films on substrates inevitably requires careful assessments of various length scales [18], over and above those encountered in the micro- or macro-indentation of bulk materials. First, the nanoindentation response of the film can be sensitive to such factors as the presence of any oxide scale, surface roughness, processing-induced surface residual stress, as well as the texture, grain size, elastic anisotropy and thickness of the film on the substrate. Second, given the small depths of indenter penetration into the thin film, the tip geometry (i.e. the shape and tip radius) of the indenter can markedly influence the indentation response, especially in the early stages of loading [18, 19]. Third, depth-sensing indentation in thin films on substrates is known to be strongly affected by the nucleation of defects and by the plastic deformation characteristics of the films which, in turn, are functions of the film thickness and microstructure (e.g. grain size, texture, etc.). For example, nanoindentation studies of polycrystalline Cu thin films on Si substrates have shown that the indentation stiffness (i.e. the slope of the P vs h plot) is a strong function of discrete deformation phenomena attributed to dislocation nucleation [18]. Despite the growing interest in the nanoindentation of thin films, very little is presently known about the microscopic deformation processes occurring beneath the indenter and their effects on the overall indentation response, from which the mechanical properties of thin films could be extracted.

The objective of the present work was to develop an understanding of the discrete and continuous deformation characteristics of thin metallic films subjected to nanoindentation. For this purpose, systematic nanoindentation experiments were conducted on polycrystalline thin films of face-centered-cubic (f.c.c.) metals of known texture and different thicknesses on Si substrates, as well as monocrystalline thin films of known orientations on Si substrates. Single crystalline and polycrystalline Al thin films were chosen for this investigation, along with the experimental results obtained from a parallel study of nanoindentation of polycrystalline Cu thin films on Si substrates [18]. Particular attention was devoted to the effects of the tip radius of the Berkovich diamond indenter on the nanoindentation response in order to account for any size dependence of indentation response on the indenter tip geometry or for any protective surface layers. Furthermore, the indentation loads and penetration depths were so chosen that the elastic deformation field of indentation was confined entirely within the film, with the substrate having no ostensible influence on the measured indentation response. The effects of film thickness on defect nucleation and plastic yield properties inferred from nanoindentation

were compared with independent experimental data available in the literature from substrate curvature and X-ray diffraction studies of deformed thin films. An attempt is also made to develop a mechanistic understanding of nanoindentation of thin films by recourse to observations in the transmission electron microscope (TEM) and atomic force microscope (AFM).

2. MATERIALS AND EXPERIMENTAL METHODS

Polycrystalline Al films were fabricated in the Microsystems Technology Laboratory (MTL) at the Massachusetts Institute of Technology (MIT). Silicon wafers of (100) orientation were dry oxidized at 1000°C in order to grow an oxide layer of SiO₂, approximately 100 nm in thickness, on both sides. The Al films were sputter deposited at 50°C to thicknesses of $t_f = 400, 600$ and 1000 nm. The average grain size was approximately equal to the film thickness, with the range of grain sizes spanning 400–2000 nm. Approximately 80% of the grains had a (111) texture. Transmission electron microscopy of the as-deposited films was conducted using standard dimpling and ion milling procedures. Figure 1(a) shows the plan view, as observed in the TEM, of the Al film of 400 nm thickness, indicating the grain structure. A cross-sectional TEM view of the same film is shown in Fig. 1(b), where the grain structure of the film, and the uniform interlayer of amorphous SiO₂ between the Al film and the Si substrate can be seen. Figure 1(c) reveals a uniform, native oxide layer on the surface of the Al film, approximately 5 nm in thickness.

Figure 2(a) is a TEM image of the surface of the 1 μm thick Al film in which the grain size ranges from 0.4 to 2.0 μm . Unlike those of the thinner Al films, the grains of the 1 μm thick Al film were populated with a high density of dislocations; Fig. 2(b) is a typical TEM image showing this trend. All Al thin films contained an Al₂O₃ layer on the surface which was approximately 5 nm thick.

Single crystal Al films were produced in the MicroFabrication Shared Experimental Facility in the Center for Materials Science and Engineering at MIT. Single crystal Al films (see ref. [20] for details on film processing) were epitaxially grown from the vapor phase on to NaCl substrates of (100), (111) and (133) orientation, at a substrate temperature of 350°C, to a film thickness $t_f = 400$ nm, such that the resulting films had the same orientations as the respective substrates. The film–substrate ensembles were then placed in deionized water at room temperature in order to dissolve the NaCl. The floating films were “scooped up” with oxidized Si wafers. The Al–SiO₂–Si systems were then spin-dried, and annealed at 575°C in order to reduce the SiO₂ to Al₂O₃, thereby bonding the film to the wafer. The fully bonded systems were finally cooled to room temperature.

The polycrystalline Cu films [18], for which comparisons are made with the nanoindentation studies on aluminium, were sputter deposited at 50°C to thicknesses of $t_f = 300, 600$ and 1000 nm, then vacuum annealed at 475°C for 1 h. The films had 80–90% of the grains of (111) orientation, and the rest of random orientation, with a grain size range of 0.5–2.0 μm (see ref. [18] for further details). Figures 3(a) and (b) are typical TEM images of the plan

view of the Cu film, showing the grain structure and the presence of twins. The grains exhibited very little initial dislocation density. The elastic constants, c_{ij} , of Al and Cu are listed in Table 1. These were used to calculate the elastic modulus, E_{hkl} , and the Poisson's ratio, ν , for different crystallographic orientations.

Nanoindentation experiments on polycrystalline Al films were performed using a Nanoinstruments

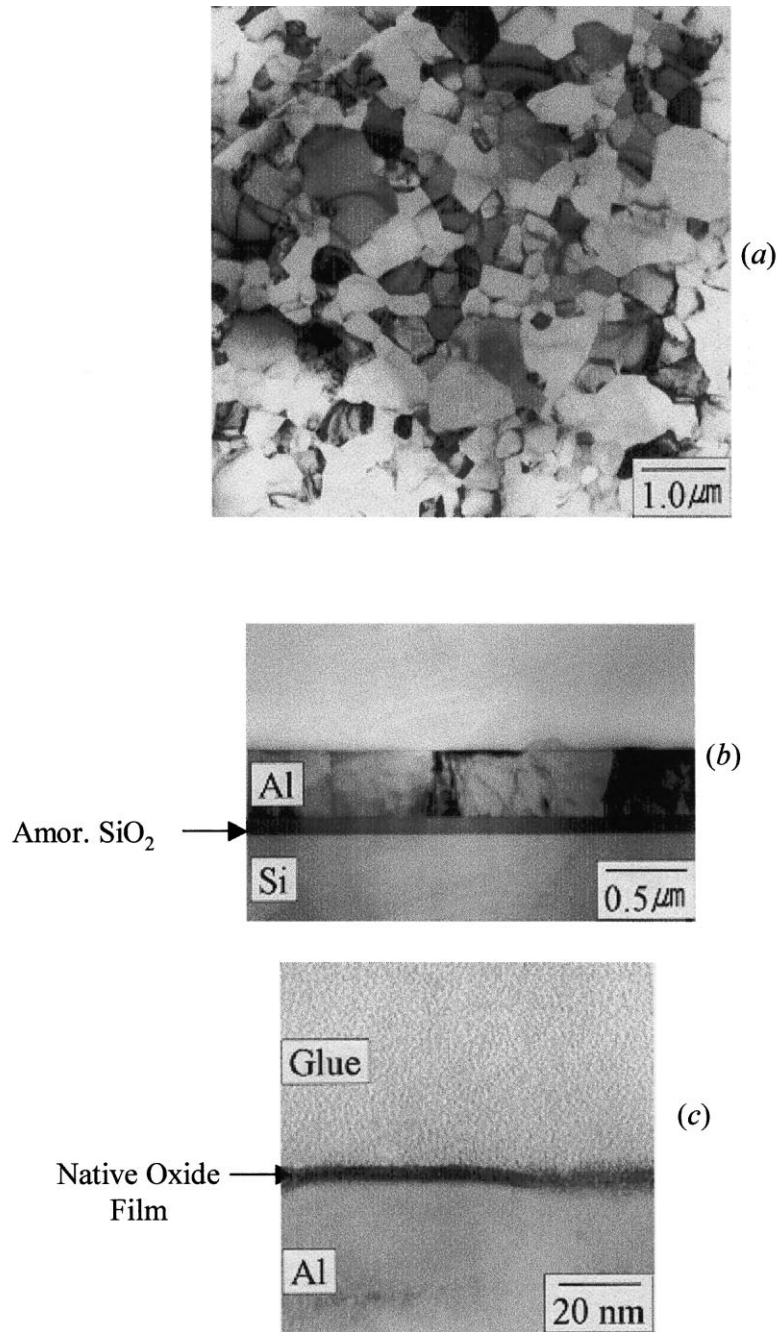
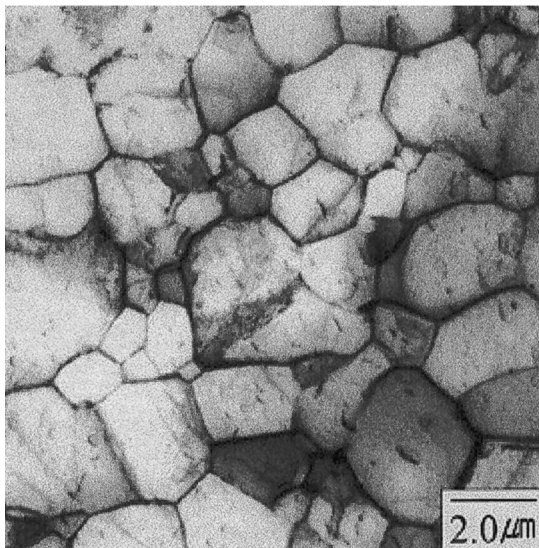


Fig. 1. (a) In-plane TEM image of the as-deposited Al film, of 400 nm thickness, on Si substrates. The grain structure has a relatively small initial dislocation density. Cross-sectional TEM image showing (b) a thin layer of amorphous SiO_2 between Al and Si and (c) approximately 5 nm thick protective Al_2O_3 on the surface of Al.

(a)



(b)

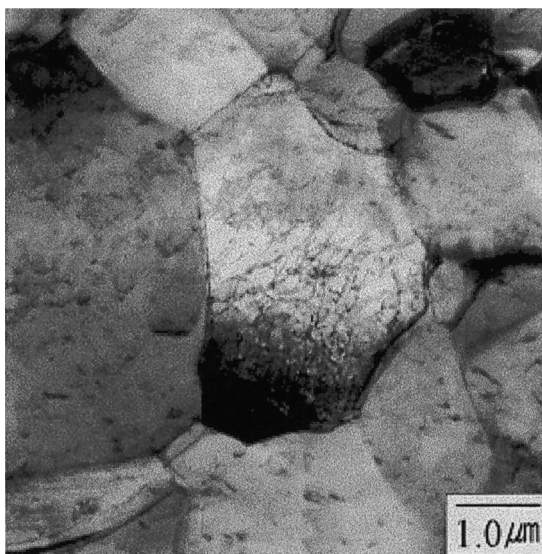


Fig. 2. (a) In-plane TEM image of the as-deposited Al film, of 1 μm thickness, on Si substrate. (b) A TEM image showing a high density of dislocations within a grain of the as-deposited film.

Nanoindenter IITM (Nanoinstruments, Inc., Tennessee, USA). A Berkovich indenter was used to indent the films. This diamond indenter, although nominally sharp, had a finite tip radius $R \approx 40\text{--}50\text{ nm}$. Figure 4 is a scanning electron micrograph of the tip of the Berkovich indenter tip used in the experiments. The sharpness and symmetry of the diamond tip are evident in this micrograph.

Nanoindentation experiments were conducted to a maximum load of $P = 0.1\text{ mN}$. The loading and

unloading phases of indentation were carried out over a time span of approximately 20 s in all the experiments. At the maximum load, a dwell period of 20 s was imposed before unloading, and another dwell period of 20 s at 90% of unloading, so as to correct for any thermal drift in the system. At least 20 indents were made for each specimen, with the adjacent indents separated by at least 10 μm . The indents were examined using a commercial atomic force microscope.

The effect of tip radius on the elastic indentation response of a material can be probed using classical Hertzian analysis [17–19]. A similar analysis was performed for the current experiments, but with the purpose of determining the depth of penetration beyond which the indenter could be treated as “sharp”. This transition depth, h_t , was calculated as a function of the included tip semi-angle, α , and tip radius, R , of the indenter.

(a)



(b)

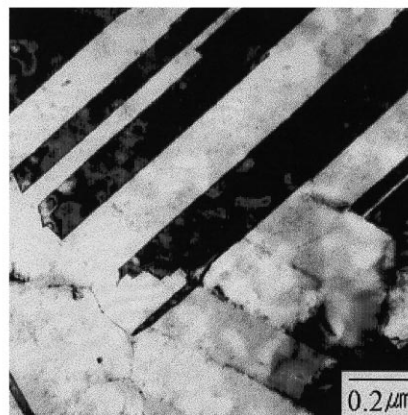


Fig. 3. (a) A transmission electron micrograph of the as-deposited Cu film showing the grain structure which is relatively free of dislocations. Annealing twins are seen in the central grain of (a) and in (b).

Table 1. Elastic constants for the materials used^a

| Material | c_{11} (GPa) | c_{12} (GPa) | c_{44} (GPa) | $E_{\text{polycrystal}}$ (GPa) | $\nu_{\text{polycrystal}}$ |
|--------------------------------|----------------|----------------|----------------|--------------------------------|----------------------------|
| Al | 108.2 | 61.3 | 28.5 | 69 | 0.33 |
| Cu | 168.4 | 121.4 | 75.4 | 132 | 0.33 |
| Diamond | — | — | — | 1000 | 0.07 |
| Al ₂ O ₃ | — | — | — | 380 | 0.16 |

^a $1/E_{hkl} = \{[(c_{11} + c_{12})(c_{11} - c_{12})(c_{11} + 2c_{12})] - 2\{[1/(c_{11} - c_{12})] - (1/2c_{44})\}(l_1^2 l_2^2 + l_1^2 l_3^2 + l_2^2 l_3^2)\}$, $\nu = c_{12}/(c_{11} + c_{12})$ where E_{hkl} = Young's modulus in the crystallographic direction $[hkl]$, l_i = direction cosine between $[hkl]$ and the cube axis x_i , ν = Poisson's ratio.

Figure 5(a) is a schematic of a nominally sharp tip (with radial symmetry), showing the effect of the indenter tip angle α on the transition depth of penetration h_t (beyond which the Berkovich indenter with a tip radius, $R \approx 50$ nm, could be analyzed as a “sharp” indenter). For an indenter with $\alpha = 25^\circ$ (e.g. [10]), $h_t = 1.6 R$, whereas for a Berkovich indenter (approximated as a conical indenter) with $\alpha = 75^\circ$, $h_t = 0.09 R$. In other words, the indenter tip radius R is expected to influence the indentation response only up to a penetration depth of $0.09R$ which, for the present experiments, is only about 4.5 nm. Therefore, the elastic portion of the P – h curve for a spherical indenter [6] where

$$P = \frac{4}{3} R^{1/2} E^* h^{3/2},$$

$$E^* = \left(\frac{1 - \nu_f^2}{E_f} + \frac{1 - \nu_i^2}{E_i} \right)^{-1}, \quad (1)$$

would only be valid for the very early stages of the present experiments. The effective modulus, E^* is defined in terms of the elastic moduli of the indenter and the film, E_i and E_f , respectively, and Poisson's ratio for the indenter and film, ν_i and ν_f , respectively. For $h > h_t$, the P – h relation for a sharp Berkovich indenter [7]

$$P = C' h^2 = 2.1891(1 - 0.21\nu_f - 0.01\nu_f^2 - 0.41\nu_f^3) E^* h^2, \quad (2)$$

should be used to describe the elastic response.

Figure 5(b) shows a series of representative

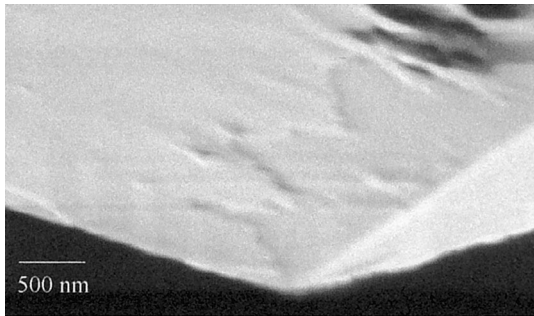


Fig. 4. A scanning electron micrograph showing the sharpness and symmetry of the Berkovich indenter tip used in the nanoindentation experiments.

results for the indentation of an elastic material with effective modulus $E^* = 100$ GPa. The load P (in mN) is plotted against h (in nm) for a sharp Berkovich indenter and three Berkovich indenters having tip radii $R = 50, 100$ and 150 nm. Each P – h curve for a rounded indenter is truncated at its appropriate value of h_t . The response for the tip radius R of 50 nm (appropriate for the experiments) is truncated at $h_t \approx 4.5$ nm. Such truncations were used when analyzing current experimental indentation data.

Nanoindentation experiments on single crystal Al films and polycrystalline Cu films [18] were also performed, under load control, using a Nanoindenter IITM (NanoInstruments, Tennessee, USA) with a diamond Berkovich indenter. In addition, a Dynamic Contact ModuleTM (DCM) was placed in series with the load train, allowing better load and depth resolution at smaller depths of indentation [21]. The tip radius of this indenter was also 50 nm. Films were indented to a maximum load of $P = 0.07$ mN and the resulting P – h curves were measured.

Nanoindentation results only up to a penetration depth $h \leq t_f/10$ were considered in all analyses, where t_f is the thickness of the Al or Cu film on the Si substrate. Thin foils, prepared from some of the indented films on substrates, were also examined in the TEM in order to assess the microscopic deformation processes introduced by nanoindentation.

3. EXPERIMENTAL OBSERVATIONS

Figure 6 shows the variation of indentation load, P , as a function of the penetration depth, h , for the three film thicknesses of polycrystalline Al on Si. All three curves exhibit abrupt bursts in displacement, separated by regions of positive slope. The indentation compliance, as seen by the slope of the P vs h plot, is not significantly affected by film thickness prior to the first burst. The load at which the first displacement burst occurs also does not appear to vary significantly with film thickness, t_f . However, the ratio $P_{\text{max}}/h_{\text{max}}$ generally decreases with increasing film thickness. Note that the maximum depth of penetration, h_{max} , was restricted to a value typically smaller than 10% of the film's thickness, t_f , in order to preclude any effects of the substrate on the indentation response.

Figure 7 illustrates the P – h curves for the three

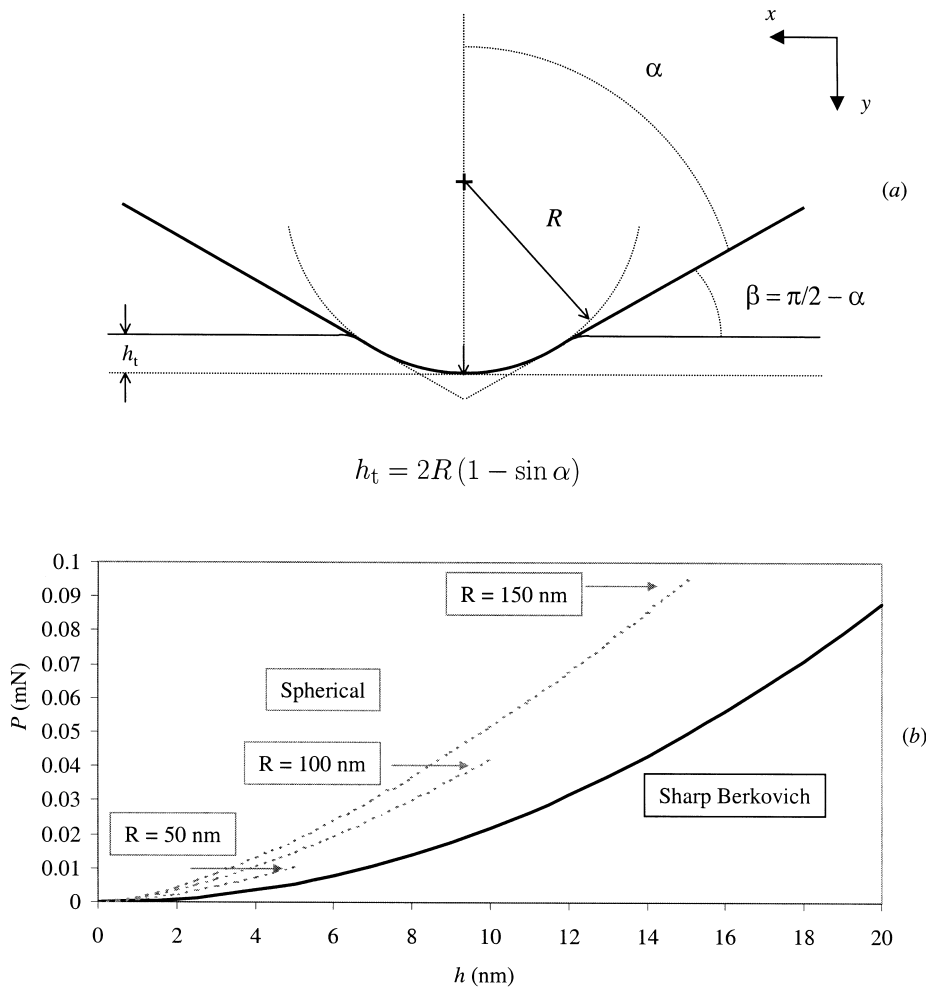


Fig. 5. (a) A schematic of the idealization of the indenter tip as a sphere and the associated nomenclature. (b) Predictions of the effects of tip radius and shape on the elastic indentation response. The curves for different radii of the spherical tip are terminated at $h = h_t$. See text for details.

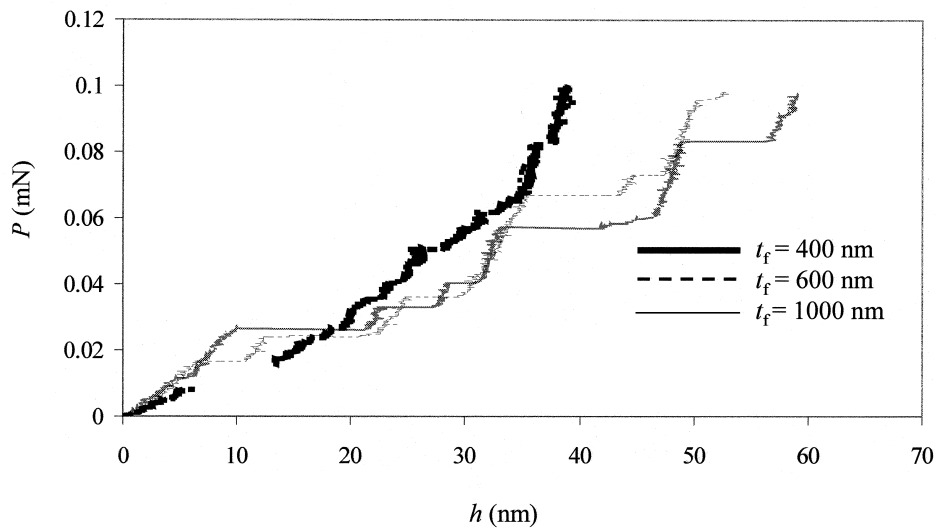


Fig. 6. Effects of thin film thickness on the nanoindentation response of polycrystalline Al.

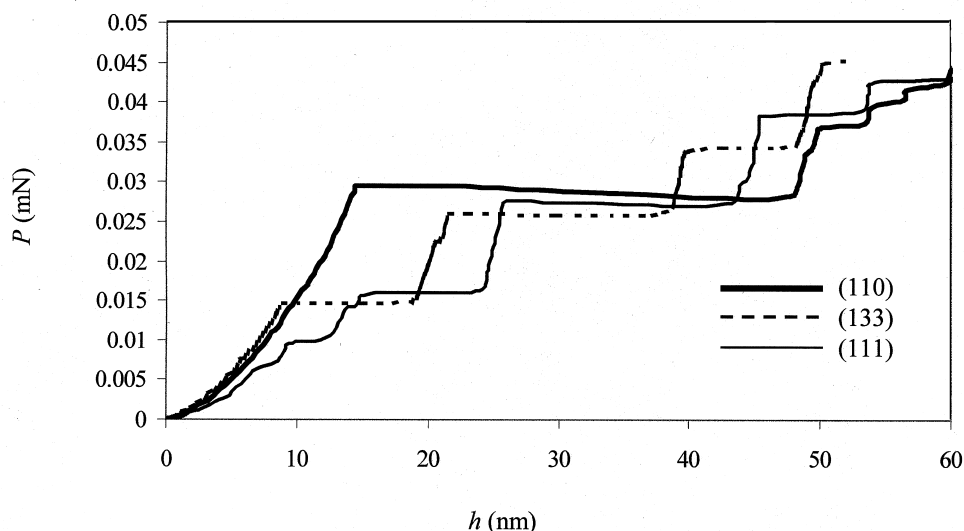


Fig. 7. Nanoindentation response of single crystal Al films of (110), (133) and (111) orientation.

orientations of single crystal Al films. As in the case of the polycrystalline Al, the plots show clearly defined displacement bursts, separated by regions of positive slope. Similar plots for the three film thicknesses of polycrystalline Cu, from ref. [18], are shown in Fig. 8. The indentation response of polycrystalline Cu is similar to that of polycrystalline Al for the different film thicknesses.

Figure 9(a) is an AFM image of the nanoindentation on the surface of the 400 nm thick polycrystalline Al film, where several surface grains are seen to be covered by the contact area. The sharpness of the triangular profile of the Berkovich tip impression, upon unloading from a maximum load of 0.1 mN, along with the pile-up of Al around the indenter (yellow regions along the indentation perimeter) are also evident in the AFM image shown for the same material [Figs 9(b) and (c)].

Transmission electron microscopy of indented polycrystalline aluminium films did not reveal features which were distinctly different from those seen in the as-deposited films (Figs 1 and 2). This was mostly attributed to the experimental difficulties in preparing TEM foils from the indented Al thin films on Si substrates; in these foils, the damage immediately surrounding the indentation could not be reliably documented. A considerable difference was repeatedly observed, however, between the indented and as-deposited Cu thin films in the TEM. Figures 10(a) and (b) are TEM images of polycrystalline Cu, taken after an indentation at $h_{\max} \approx 200$ nm, where the indented region (in the form of a triangular impression) is seen at the center of the micrograph. The white region in the middle of the indentation corresponds to amorphous SiO_2 . Note that the perimeter of the indented region is popu-

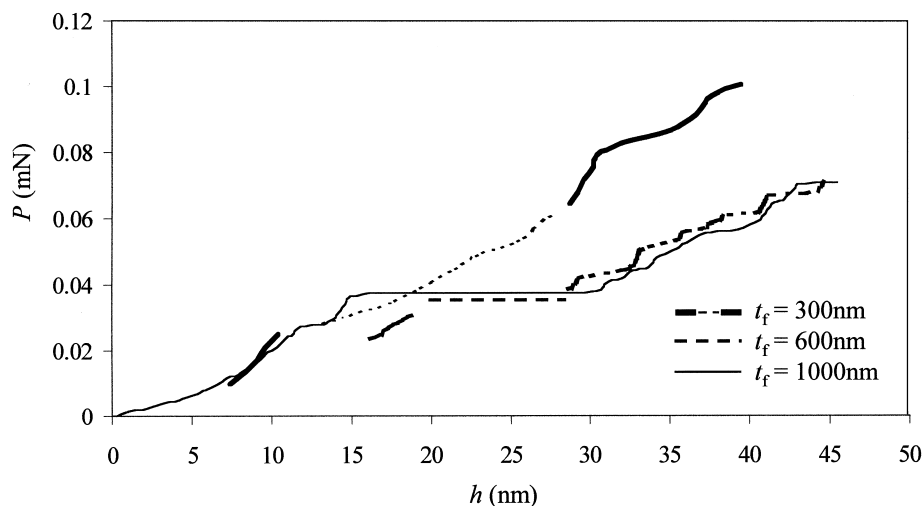


Fig. 8. Effects of thin film thickness on the nanoindentation response of polycrystalline Cu [18].

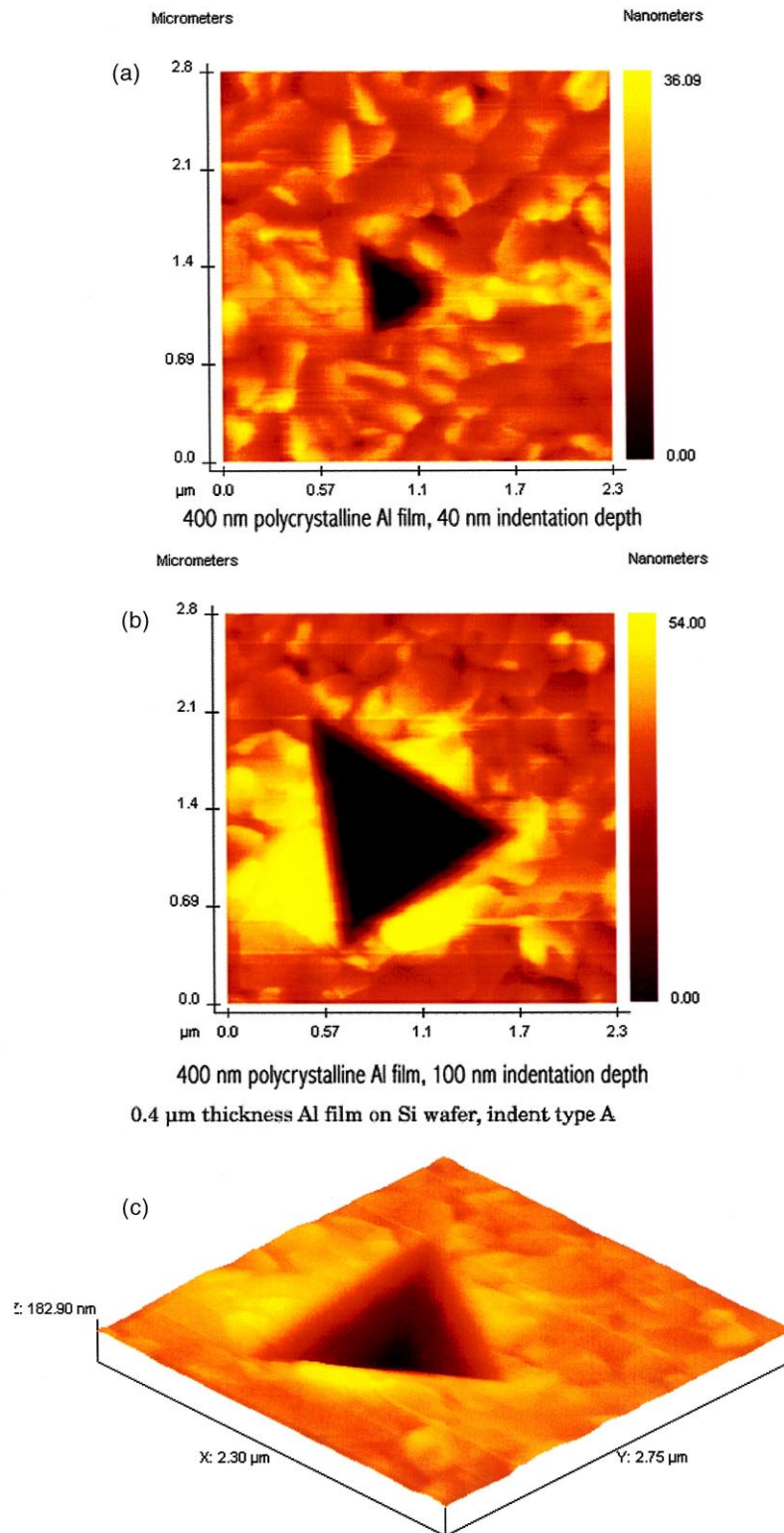


Fig. 9. (a) AFM image of nanoindentation on 400 nm polycrystalline Al thin film. Indentation depth = 40 nm. The color marker on the right side of (a) and (b) refers to the surface uplift in nm. (b) Indentation depth = 100 nm. Note the pile-up of material (yellow region) around indentation. (c) A three-dimensional view of the “sharp” Berkovich indentation.

lated with a high density of dislocations; however, essentially no dislocations are visible in regions far removed from the indentation (just as in the case of the as-deposited, unindented Cu film shown in Fig. 3). In the central portion of the lower half of Fig. 10(b), rows of dislocations are evident, extending outward from the indentation into an adjacent grain. The dislocations lie between a grain boundary and a twin boundary. A higher magnification view of this dislocation arrangement is shown in Fig. 10(c). At distances far away from the indented region, i.e. at distances of 5–10 times the average diameter of the indentation contact region, no such dislocation structure is visible, as shown in Fig. 10(d). Here, only the twin structures, similar to those seen in the as-deposited Cu film (Fig. 3), are noticeable.

4. DISCUSSION

All of the indentation responses observed in this study on monocrystalline and polycrystalline Al and polycrystalline Cu thin films on substrates exhibited bursts in indenter displacement into the film, which were separated by regions of positive slope. We present here a method of interpreting these experiments.

4.1. Overall classification of nanoindentation response

Figure 11(a) shows a schematic of a typical P - h curve produced in the present nanoindentation experiments. The representative curve contains parabolic sections, separated by plateaus that represent displacement bursts. Two particular features of this

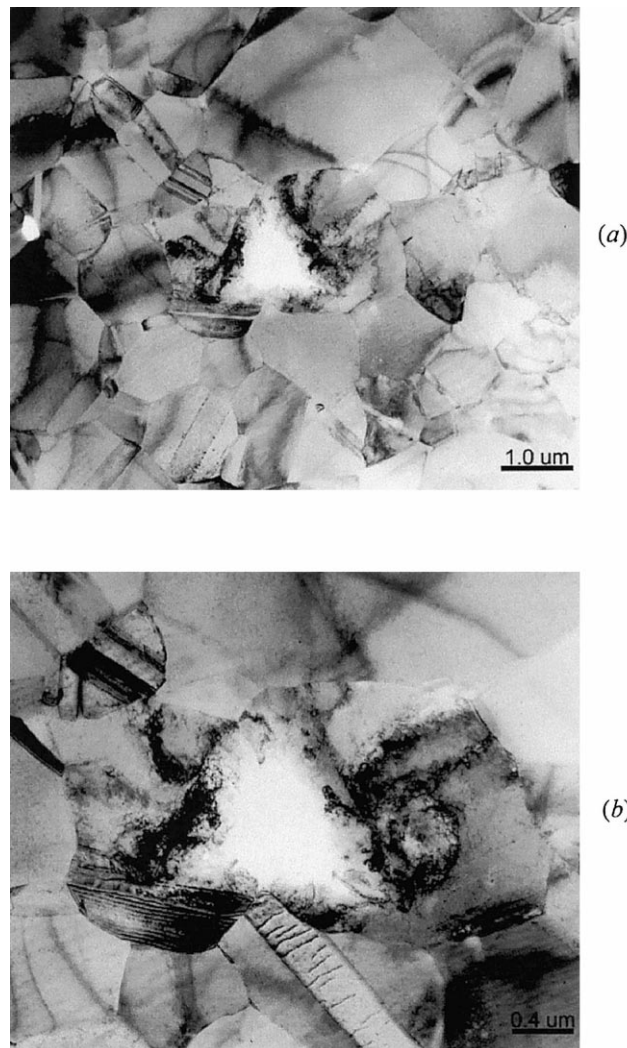


Fig. 10. (a), (b) TEM images, at two different magnifications of the indented polycrystalline Cu film. Note the high dislocation density induced around the indentation and the dislocation-free grains far away from indentation. Indentation depth = 200 nm. (c) A higher magnification image of the grain beneath the indentation in (b) into which dislocations are punched out by interaction. (d) Twinning in grains far away from indentation.

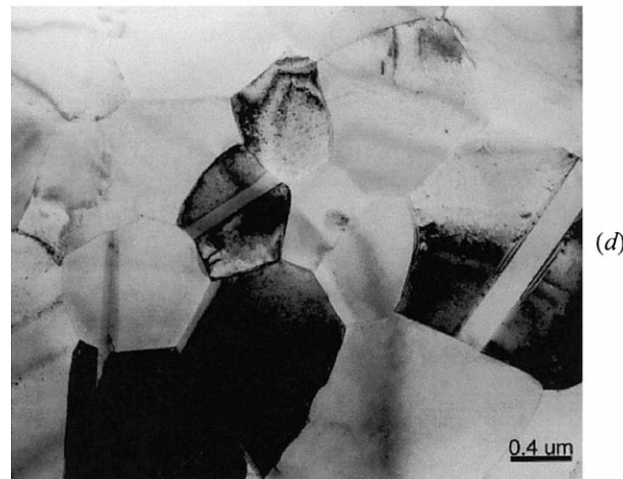
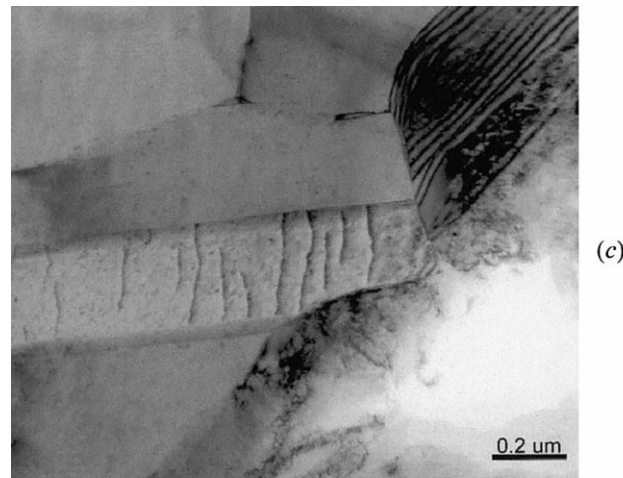


Fig. 10 (continued)

curve are apparent. First, as shown in Fig. 11(b), a parabola, described by the Kick's law, equation (2), can be fitted between the (P, H) points, $(0, 0)$ and (h_{\max}, P_{\max}) bounding, to the right, the bursts in displacements. This bound could be constructed as representing the overall elastoplastic response of the thin film which, from the present experimental results, is seen to be a function of the film thickness. Second, if the bursts are removed from the plot, and the curves between the plateaus moved accordingly in the direction of the arrows, a single consolidated parabola, Fig. 11(c), results representing the elastic response of the indented film at low loads (where there is no influence from the substrate). Thus, the P - h curves merely represent a broken parabola—an elastic parabola separated by displacement bursts. The consolidated experimental P - h curves (with jumps removed) thus match the theoretical elastic parabola for sharp elastic

Berkovich indentation [equation (2)]. In other words, this consolidated curve could be constructed solely from knowledge of the elastic properties of the thin film and the indenter by recourse to equation (2).

4.2. Analysis of elastic indentation stiffness

Figure 12 shows the consolidated elastic curves generated following the procedure outline in Fig. 11(c) for the three polycrystalline Al thin films from the nanoindentation test results presented in Fig. 6. Plotted along with the experimental curves is the theoretically predicted elastic indentation response from equation (2), for a sharp Berkovich indenter. Also plotted are three curves, representing equation (1), for a spherical indenter tip with radius $R = 25, 50$ and 100 nm. The predicted curves for the spherical tip are all truncated at their appropri-

ate values of h_t . The value of E^* used for the theoretical curves was 74 GPa, as calculated from equation (1), using the values $E_f = 69$ GPa (for polycrystalline Al film), $E_i = 1000$ GPa for the diamond indenter, and $\nu_f = 0.3$ and $\nu_i = 0.07$ for film and indenter, respectively. [Due to the varying grain size relative to indentation area, typically one to several grains were sampled during each test. Therefore, the elastic response essentially reflected that for a single crystal of (111) orientation.] It can be seen that the consolidated curves are in reasonable agreement with the predicted sharp indenter elastic response, and that the curves show little dependence on film thickness, t_f . A similar match between predicted elastic response between the displacement bursts and the nanoindentation experimental results was also seen for polycrystalline Cu thin films on Si substrates [18].

Since Al is invariably covered with native Al_2O_3 layers, typically about 5 nm in thickness, it is also of interest to examine the effect of such native oxide films on the initial slopes of the P - h curves. For this reason, Fig. 12 also includes a plot of equation (1) for a spherical indenter with tip radius

$R = 50$ nm, indenting an elastic material (Al_2O_3) having an $E^* = 280$ GPa. It is apparent that this curve does not fit well with the experimental results, and supports the inference that any influence of the thin oxide layer would be confined to the very early stages (≤ 5 nm) of the indenter penetration into the film.

Figures 13(a) and (b) show the indentation responses for the single crystal Al films of (110) and (133) orientations, respectively. In this case, the curves are presented in their original form for clarity, with the elastic portion of indentation, equation (2), superimposed on the experimental data at the end of each burst in displacement. For each parabola, a value of E^* was calculated for the particular single crystal orientation, following an analysis of indentation of anisotropic crystals given in [22, 23]. The elastic response, predicted using $E^* = 74$ GPa, is seen to match the experimental results very well. The results for the (111) single crystal ($E^* = 74.9$ GPa) were similar; they are not shown here because of space restrictions.

4.3. Effects of film thickness on overall elastoplastic response

The present experiments reveal (see Figs 6 and 8), as anticipated, that the elastic response of the films is independent of thickness, t_f , as is the value of P at which the first burst occurs. However, as the indentation depth increases, film thickness is found to have an effect on elastoplastic response of the material under indentation. Referring to Fig. 11(b), the indentation response can be shown to approach a parabolic, consolidated elastoplastic curve, the functional form of which is $P = Ch^2$, and the endpoints of which are $(0, 0)$ and (h_{\max}, P_{\max}) , bounding the bursts of displacements on the right. For both sets of polycrystalline films tested, the average value of C decreases with film thickness, at a fixed P_{\max} . At higher P_{\max} , C decreases further, but with the same dependence on film thickness. In a typical Berkovich indentation test, the macroscopic parabolic indentation response of a metallic thin film (assuming no strain hardening) can be related to the film yield strength, σ_y , by the relation [7]

$$C = 12.0348\sigma_y \left[1 + \ln \frac{E^* \tan 24.7^\circ}{3\sigma_y} \right]. \quad (3)$$

If the observed values of C for the polycrystalline Al and Cu nanoindentation experiments are interpreted using equation (3), the resulting plot of σ_y vs $1/t_f$ for both materials is shown in Fig. 14. In order to compare the two sets of experiments correctly, P_{\max} was chosen as 0.07 mN for both sets of films.

Several trends are extracted from Fig. 14. First, for both Al and Cu, σ_y increases with $1/t_f$. Second, the absolute values of σ_y for Cu films are shown to be greater than those for Al, which would be

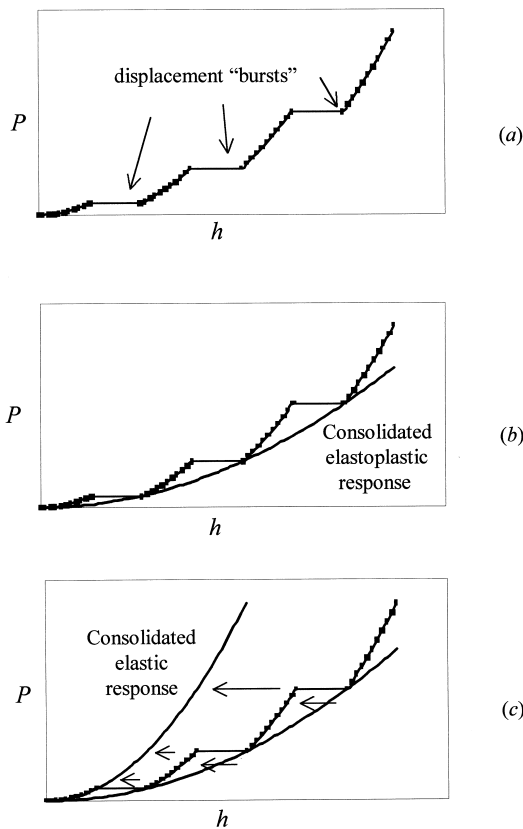


Fig. 11. (a) Nanoindentation responses showing displacement bursts. (b) Consolidated elastoplastic parabola constructed through maximum displacements. (c) Bursts removed to construct a consolidated elastic parabola.

expected on the basis of previous investigations into the yield strength of thin films [24–29]. Also shown in Fig. 14 are the yield strength values, σ_y , of Al and Cu films, as functions of inverse film thickness, $1/t_f$, obtained on the basis of independent experimental measurements involving substrate curvature changes during thermal cycling or X-ray diffraction measurements [24–29]. Several general trends could be extracted from this comparison. The nanoindentation experiments show that the overall (macroscopic) yield strength of thin films on substrates generally increases with decreasing film thickness, for the range of thicknesses examined here, for both Al and Cu. This trend is qualitatively consistent with the inference made from curvature and X-ray diffraction measurements of thin films [24–29]. The approximate yield strength shown in Fig. 14 from nanoindentation, however, is several times higher than that estimated from the other techniques.

This apparent discrepancy can be attributed to several major differences between these different experimental methods. First, the indentation results depend strongly on the level of load (P_{\max}), which denotes an indentation size effect. Second, the overall plastic response, as defined in the consolidated elastoplastic curve in Fig. 11(b), comprises not only microplasticity arising from discrete displacement

bursts (which is linked in the following sections to dislocations), but also the elastic deformation that separates the bursts. As a result, the ensuing estimation of an overall yield response would be expected to be higher than that arising solely from any macroscopic plasticity. Third, the nanoindentation response probes highly localized deformation at very low loads, whereas substrate curvature experiments sample an average, macroscopic deformation response. Fourth, nanoindentation experiments are conducted at constant (room) temperature, whereas curvature and diffraction experiments are generally carried out during cyclic variations in temperature introduced with the objective of inducing thermal mismatch stresses in the films. As a result, the ensuing inelastic deformation that arises in the latter experiments could be affected by dislocation plasticity, as well as thermally activated processes such as diffusion or grain boundary sliding. Temperature-dependence of yield strength also becomes a complication in the interpretation of such experiments. Fifth, in all these experimental methods, including the present nanoindentation study, pre-existing residual stresses could influence plastic deformation response; such effects of residual stresses are not incorporated into the analyses of experimental data.

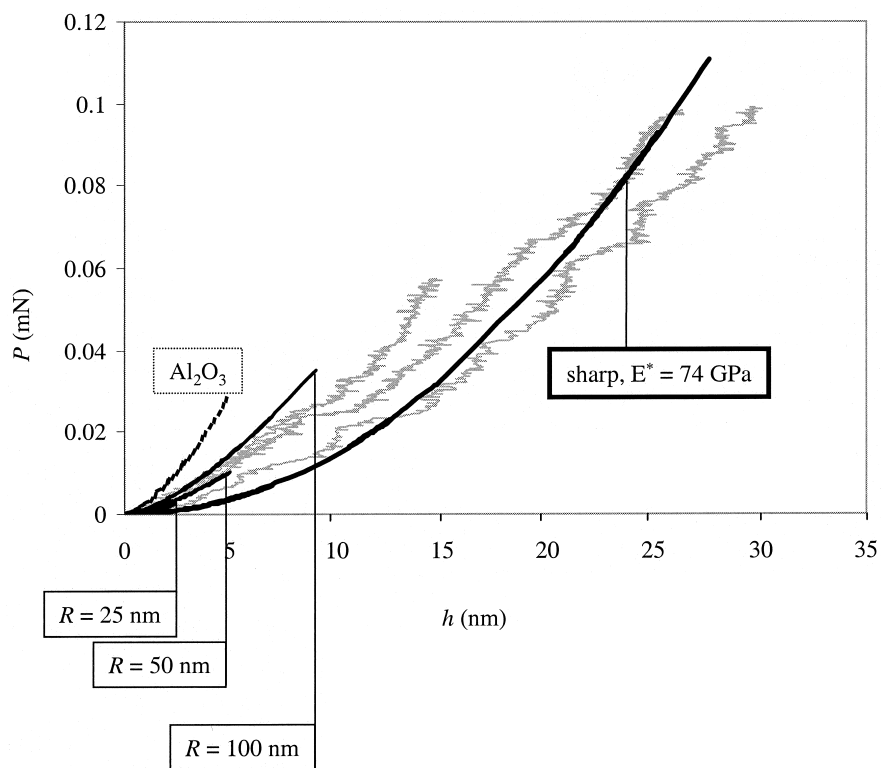


Fig. 12. Consolidated elastic indentation response for polycrystalline Al, plotted for the sharp Berkovich indentation of an elastic material (Al) with $E^* = 74$ GPa. The curves denoted as “shifted by δ ” account for the extra depth δ which is depicted in Fig. 5(a). Also included are curves corresponding to spherical indentation with $R = 25, 50$ and 100 nm, and for Al_2O_3 of 5 nm thickness ($R = 50$ nm).

Figures 15 and 16 show the consolidated elastic as well as elastoplastic indentation responses of polycrystalline Al and Cu thin films, respectively, on Si substrates, as functions of film thickness. In these figures, the elastic response represents the load vs displacement plots where the displacement bursts are removed, and the elastoplastic response represents the consolidated, right-bounding curve, following the procedure outlined in Fig. 11(b). Also shown for comparison in Figs 15 and 16 are the elastic and plastic properties of bulk Al and Cu. Whereas the elastic response of the metals is unaffected by film thickness, the consolidated elastoplastic response is seen to be a strong function of film thickness, with increasing film thickness resulting in a more compliant indentation response.

It is emphasized here that the results of nanoindentation should primarily be used as a relative measure of the dependence of film thickness on yield strength and not as an absolute measurement of the yield strength. At low loads, both local plastic deformation and elastic deformation influence indentation stiffness; consequently, the results do not represent macroscopic yield properties of the film. While higher indentation loads could possibly render the plastic response closer to that seen in other experimental methods, deeper penetration of the indenter into the film (than those considered in this work) could incorporate the effects of substrate deformation into the indentation response, thereby complicating the interpretation of results. Thus, possible substrate effects currently place a limit on h_{\max} .

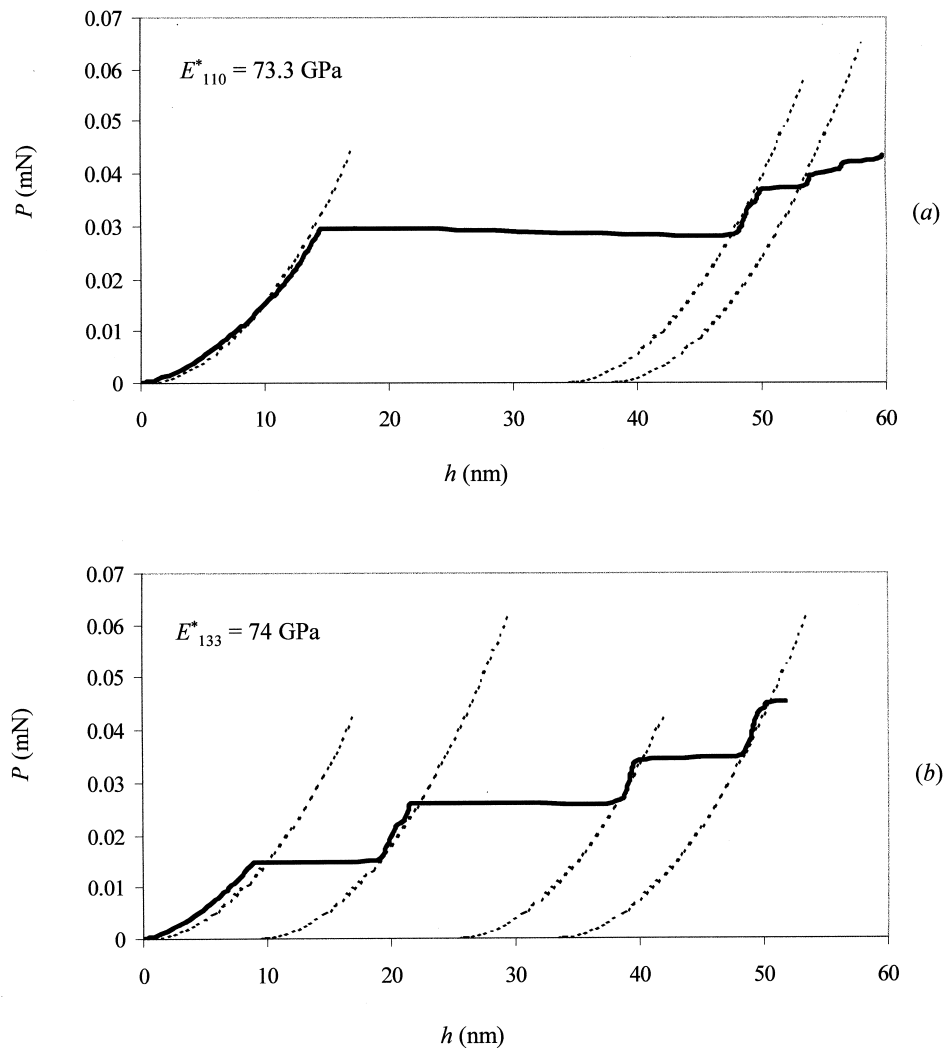


Fig. 13. Experimentally observed indentation response of single crystal Al films of two orientations, (a) (110) and (b) (133), with the theoretically predicted elastic response, equation (2), representing sharp elastic Berkovich indentation superimposed as the dotted curves.

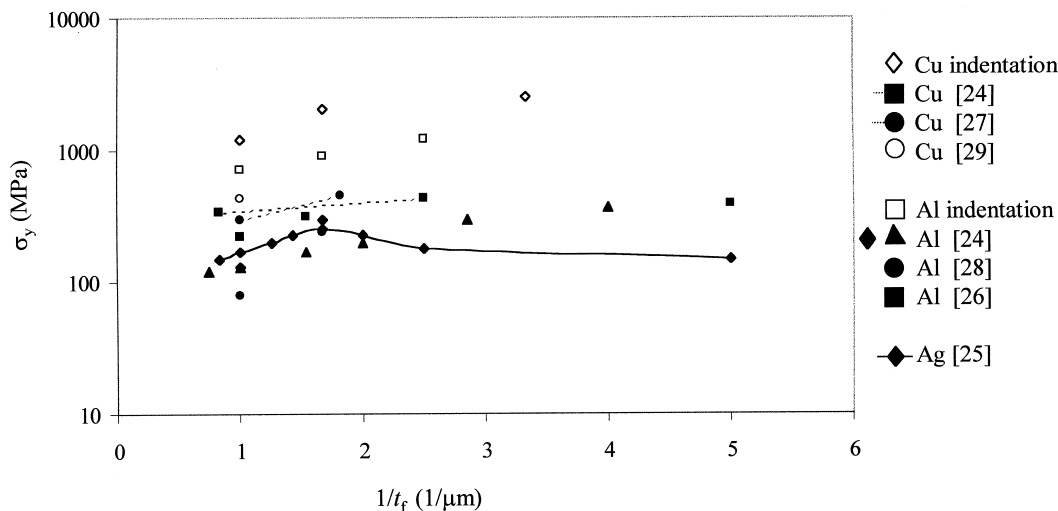


Fig. 14. A comparison of the yield strength of f.c.c. metal films as a function of inverse film thickness, as estimated from the present nanoindentation experiment and from curvature/X-ray diffraction techniques. $P_{\max} = 0.07$ mN.

4.4. On microplasticity in thin films subjected to nanoindentation

Figures 11–13 clearly reveal that the parabolic sections of the indentation response between two successive “bursts” in displacements could be attributed to purely elastic deformation in the film. In this section, we consider the origins of such displacement bursts and explore the conditions for their nucleation.

It has been postulated in some previous investigations (e.g. [1]) on the indentation of bulk materials that the displacement bursts seen upon loading could be attributed to (i) the cracking of the indented film, (ii) the cracking of a native oxide layer present on the surface, or (iii) the nucleation and motion of dislocations under the

indenter. The AFM images shown in Figs 9(a)–(c), as well as other related observations at high magnifications, do not reveal any film cracking in all present experiments. The TEM images of the Al films, such as Fig. 1(c), show a 5 nm thick native oxide on the surface. The periodic bursts, which occur both in single crystal and polycrystal Al films, persist to penetration depths of tens of nm, and even the initial burst extends to 25 nm or so. In addition, any cracking of a stiff oxide layer would result in a decrease in load, as load would be transferred to the underlying, more compliant metallic film, and hence would not lead to a plateau in the load–displacement curve. Furthermore, the indentation response separating the displacement bursts exhibits a parabolic slope, which can be predicted solely

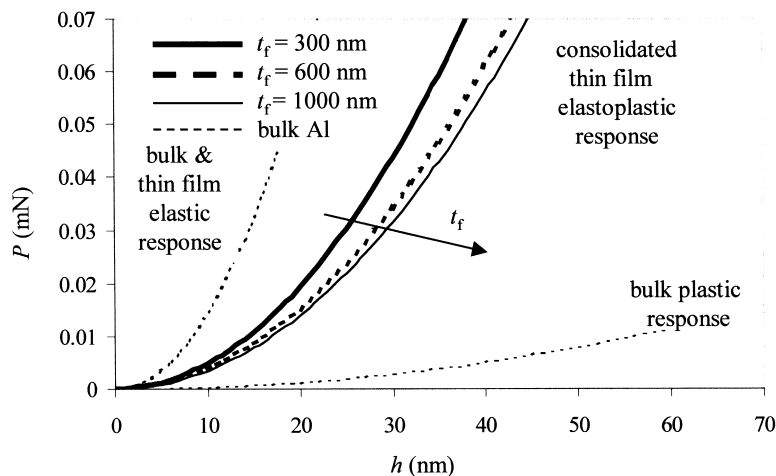


Fig. 15. Consolidated elastic and elastoplastic response of polycrystalline thin film Al to nanoindentation and comparison with bulk Al.

from the elastic properties of the thin film (see Figs 12 and 13). It is also worth noting that other investigations of nanoindentation on noble metals such as Au, Pt and Ir have also documented very pronounced displacement bursts [10, 30]. In view of these observations, it is concluded that while protective oxide layers could influence nanoindentation response in the very early stages of loading (see Fig. 12), any cracking of such protective layers does not appear to be the primary mechanism responsible for the displacement bursts in the present experiments.

Studies of the plastic response of materials subjected to indentation have drawn an analogy between the plastic zone which expands radially beneath an indenter under the confinement of the neighboring elastic material, and an expanding cavity [31, 32]. At the dislocation level, this so-called expanding cavity model is visualized by a series of, "geometrically necessary", prismatic dislocation loops that are punched out into the material to accommodate the indenter [33, 34]. The rotation of the crystalline material around the indenter, along with the relaxation engendered by the unloading of the indenter, would then be manifested as the pile-up of the material around the indentation. This process has been analyzed by recourse to slip line field theories [35]. The rotation of the lattice arising as a consequence of the geometric need to accommodate the indenter could also be viewed as the origin of geometrically necessary dislocations, whose density varies inversely with the maximum indentation load [36–38]. [This latter process has been postulated to be one possible cause of the apparent indentation size effect (e.g. [38]).] Transmission electron microscopy of microindented MoSi₂ single crystals show that, while both these processes serve to accommodate deformation, prismatic punching of (100) and (001) dislocations immediately beneath the indenter appears to be the more dominant process [39]. The nucleation, geometry and kinetics of

dislocations induced by nanoindentation require considerable further study involving electron microscopy. However, some quantitative understanding of the mechanisms underlying the present experimental trends could be extracted by idealizing the dislocation geometry as an array of colinear prismatic loops.

In the present experiments, TEM observations of indented Cu films indicate the punching of dislocations from the indentation as well as the nucleation of a high density of dislocations surrounding the indenter (Fig. 10). Atomic force microscopy of the indented Al films also reveals pile-up of material around the indentation (Fig. 9). Insights into the conditions governing dislocation nucleation in the thin films could be gained by exploring the local stresses that arise at the tip of the indenter during the loading of the films of different thicknesses.

Consider first the load, P , at which the first displacement burst occurs during nanoindentation of polycrystalline Al and Cu. From this load, along with the geometry and elastic properties of the indenter/film system, the maximum shear stress, τ_{\max} , underneath the indenter tip is easily computed. Although the overall indentation response of the films can be treated as that arising from a sharp indenter beyond a critical penetration depth h_c , the tip radius of the indenter would be expected to influence the local stress state at low loads where the first displacement burst occurs. In the following, we examine the local stress state for both the rounded and sharp indenter tips.

The maximum elastic shear stress underneath a spherical indenter is given by the relation [6]

$$\tau_{\max} = 0.31 \left(\frac{6PE^*2}{\pi^3 R^2} \right)^{1/3}. \quad (4)$$

The experimentally observed value of P for the initial burst ranges from 0.015 to 0.027 mN for the polycrystalline Al films, and is roughly 0.035 mN for the polycrystalline Cu films. From equation (4),

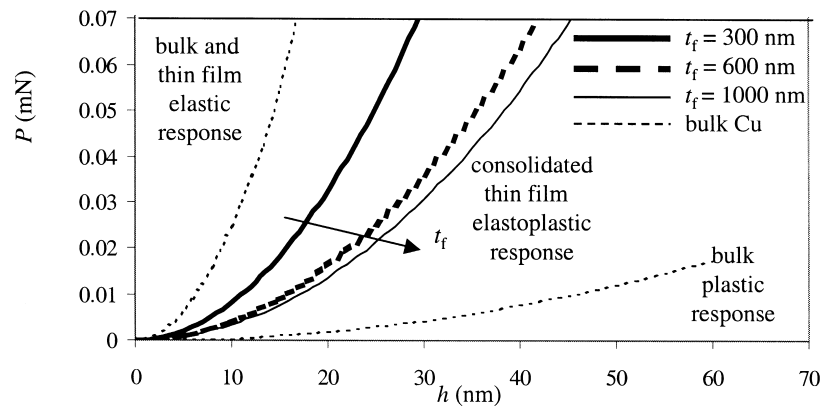


Fig. 16. Consolidated elastic and elastoplastic response of polycrystalline thin film Cu to nanoindentation and comparison with bulk Cu.

it is seen that $\tau_{\max} \approx 4.5\text{--}8.2$ GPa for Al, and 15 GPa for Cu. The theoretical shear strength of the indented material may be approximated as $\mu_s/2\pi$, where μ_s is the shear modulus. This gives a theoretical shear strength of 4.5 GPa for polycrystalline Al and 15 GPa for (111) oriented Cu. This comparison reveals that the first displacement burst for both Al and Cu apparently occurs when the maximum shear stress beneath the indenter approaches the theoretical shear strength (also see ref. [15]). A similar conclusion was drawn from the nanoindentation studies of bulk Au [10] and thin film Cu [18]. The differences between the computed τ_{\max} and the theoretical shear strength can be attributed to a number of factors, including experimental scatter, especially during the early stages of nanoindentation, surface roughness, residual stresses in the film, and the presence of defects or grain boundaries or oxide scales.

For the case of the three single crystal Al films, the initial bursts occur at $P = 0.03, 0.008$ and 0.015 mN, for the (110), (111) and (133) orientations, respectively. From equation (4), $\tau_{\max} = 8.2, 5.5$ and 6.8 GPa for these three orientations, respectively. The theoretical shear strength, when calculated to be $\mu_s/2\pi$, does not vary over such a comparable range as the values of τ_{\max} for the three orientations; it is roughly 4.5 GPa. Thus, values of τ_{\max} agree with the values of theoretical shear strength for the Al single crystals about as well as they do for the polycrystalline films.

For completeness, a similar calculation is presented next for a sharp indenter tip. The average pressure underneath a sharp Berkovich indenter in an elastic–ideally plastic material is given by the relation [7]

$$p_{\text{ave}} = \frac{P}{9.946h^2} \approx 0.196E^* \quad (5)$$

and the maximum von Mises stress underneath the indenter is $\sigma_{\text{Mises}} \approx 1.5p_{\text{ave}}$ and is not dependent upon load P , as in the case for a spherical indenter. The maximum von Mises stresses are calculated to be 21.8 GPa and 38.2 GPa for polycrystalline Al and Cu, respectively. These values could then be converted to equivalent shear stresses using the re-

lation

$$\tau_{\text{eq}} = \frac{\sigma_{\text{Mises}}}{\sqrt{3}}. \quad (6)$$

Thus, the shear stresses under the sharp indenter are 12.6 GPa and 22.0 GPa for Al and Cu, respectively, which are 50% higher than the theoretical shear strength of both materials. This comparison indicates that a stress-based criterion for dislocation nucleation and motion, which considers shear stresses underneath a tip radius R , gives a more realistic agreement between calculated stresses and material properties. These estimates are listed in Table 2 for the various films examined in this work. It should, however, be noted that these stress estimates assume an isotropic material with a geometrically flat surface; crystalline anisotropy and surface roughness could lead to considerable changes in these estimates.

4.5. A simple energetic model for dislocation emission during nanoindentation

The foregoing analyses of the correlation between the maximum shear stress under the indenter at the onset of displacement bursts and the theoretical shear strength of the material provide one physical justification for the nucleation of dislocations following the initial elastic indentation response. Another quantitative justification for not only the nucleation of dislocations, but also the width of the plateau in the P – h curves represented by the displacement bursts during nanoindentation, can be obtained by invoking the energetics of dislocation loops. For this purpose, we present a simple model which assumes that the total elastic energy stored in the thin film during the initial elastic deformation induced by nanoindentation is exhausted by the accumulation of geometrically necessary prismatic dislocation loops in such a way that it accounts for the total elastic energies of all the dislocations punched out underneath the indenter.

The model is predicated on the following simplifying assumptions: (i) The dislocation configuration is that of a simple stack of coaxial prismatic loops, which are idealized as circular, with a radius R_d .

Table 2. A comparison of predicted τ_{\max} with τ_{th} for different materials and indenters

| Material | Indenter tip shape | Predicted τ_{\max} (GPa) equations (2) or (6) | Theoretical shear strength, τ_{th} (GPa) |
|-------------------|--------------------------|--|--|
| Al polycrystal | Spherical ($R = 50$ nm) | 4.54–8.2 | 4.2 |
| | Sharp Berkovich | 12.6 | |
| Al single crystal | | | |
| [110] | Spherical ($R = 50$ nm) | 8.2 | 4.5 |
| | Sharp Berkovich | 12.6 | |
| [111] | Spherical ($R = 50$ nm) | 5.5 | 4.5 |
| | Sharp Berkovich | 12.6 | |
| [133] | Spherical ($R = 50$ nm) | 6.8 | 4.5 |
| | Sharp Berkovich | 12.6 | |
| Cu polycrystal | Spherical ($R = 50$ nm) | 15 | 15 |
| | Sharp Berkovich | 22.0 | |

This process is schematically shown in Fig. 17(a); (ii) Slip occurs in the direction of indentation with a Burgers vector of magnitude, b , and the slip direction is taken to be parallel to the $[110]$ direction of the f.c.c metal film; (iii) If Δh_b is the width of the displacement burst, as shown in Fig. 17(b), the number of prismatic loops punched out beneath the indenter, $N \approx \Delta h_b/b$. The loops are assumed to be evenly spaced through the thickness of the films, for simplicity of analysis, with the loop spacing, $\rho = t_f/N$ (where t_f is the film thickness); (iv) To a first order, the image forces and free surface/interface effects on the energies of dislocations are not considered; (v) The indented material is homogeneous and isotropic, with a geometrically perfect surface.

The total elastic energy stored in the thin film as a consequence of indentation-induced deformation is given by the shaded area in Fig. 17(b):

$$W_e = \int_0^{h_b} C' h^2 dh = \frac{C' h_b^3}{3}, \quad (7)$$

where C' is the elastic loading curvature during nanoindentation and h_b is the indenter penetration depth at which the first displacement burst and dislocation nucleation occur. The interaction energy between two coaxial, circular prismatic dislocation

loops of radius, $R_d \gg \rho$ is given by [40, 41]:

$$W_i = \frac{\mu_s b^2}{1-\nu} R_d \left(\ln \frac{8R_d}{\rho} - 1 \right), \quad (8)$$

where ν is the appropriate Poisson's ratio of the thin film. In the present case of N coaxial loops, the loop closest to the free surface interacts with the $N-1$ remaining loops, with the interaction energy becoming weaker with increasing distance from the first loop. Summation of these interactions gives the following expression for the term within the parentheses in equation (8):

$$\begin{aligned} & \sum_{j=1}^{N-1} \left(\ln \frac{8R_d}{j\rho} - 1 \right) \\ &= \ln \frac{8R_d^{(N-1)}}{(N-1)! \rho^{N-1}} + (N-1). \end{aligned} \quad (9)$$

The total energy is obtained by summation over all the loops. The second loop interacts with $(N-2)$ others [since interaction with $(N-1)$ would lead to two interactions between the first and the second loops], the third loop with $(N-3)$ others, etc. Summation over all the loops yields the relation:

$$\begin{aligned} W_i^t = \frac{\mu_s b^2}{1-\nu} R_d \left\{ \sum_{j=1}^{N-1} j \left(\ln \frac{8R_d}{\rho} \right) - \sum_{j=1}^{N-1} \ln(j!) \right. \\ \left. - \sum_{j=1}^{N-1} j \right\}. \end{aligned} \quad (10)$$

The self energy of an isolated circular dislocation loop, W_s , in an infinite medium is extracted by setting $\rho \approx b \ll R_d$ in equation (8) and by taking one half of the quantity on the right-hand side of equation (8), where the length of the loop has been counted twice:

$$W_s = \frac{\mu_s b^2}{2(1-\nu)} R_d \left(\ln \frac{8R_d}{\rho} - 1 \right). \quad (11)$$

The self energy of each loop could be regarded as the interaction energy between all segments of the loop [41]. The total self energy of N circular loops then equals $N \times W_s$. When the number of loops N is large (of the order of 50 or more, as in the present case), the overall interaction energy given by equation (10) far exceeds the total self energy term, $N \times W_s = W_s^t$.

In equation (10), μ_s and ν are known elastic constants of the thin film of known orientation, and b , N and ρ are known from the slip direction, Δh_b and film thickness, respectively. The only unknown quantity in equation (10), the radius of the prismatic dislocation loops, R_d , is solved by setting $W_e = W_i^t + W_s^t$.

Note that the above analysis could also be refor-

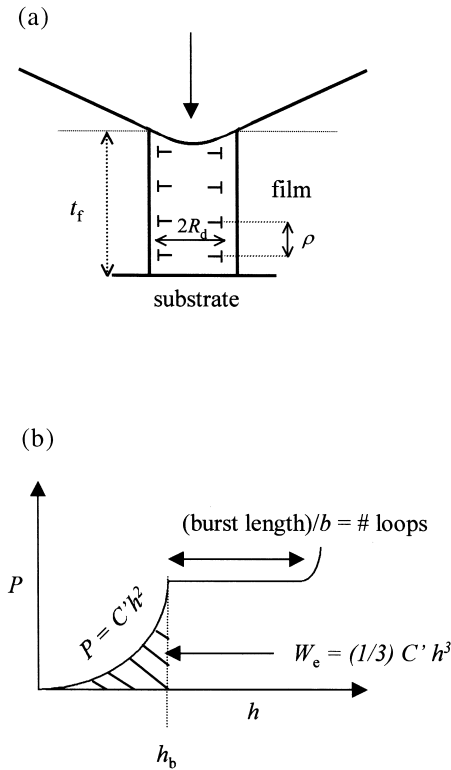


Fig. 17. (a) A schematic of colinear prismatic dislocation loops underneath an indenter in a thin film. (b) Elastic energy associated with dislocation nucleation. See text for details.

mulated in the reverse manner for predictions of the extent of displacement burst. For example, invoking the assumption that the indentation contact diameter is equal to the radius of the punched out dislocation loops, the above energy model could be solved for Δh_b .

Consider now the specific case of a (110) textured Al thin film ($b \approx 3$ nm) with $t_f = 400$ nm. From Fig. 7, note that $h_b \approx 14$ nm and $\Delta h_b \approx 30$ nm. From Fig. 7, the area under the initial elastic regime gives: $W_e \approx 1.28 \times 10^5 \text{ GPa} \cdot \text{nm}^3 = W_i^1$. Using this result in equation (10) along with the elastic properties of Al and solving for the dislocation loop radius gives $R_d \approx 37$ nm. This value is roughly equal to the contact radius under the Berkovich indenter, corresponding to the onset of the first displacement burst at a penetration depth of 14 nm. Thus, the simple dislocation model is seen to provide dislocation dimensions that are of the correct length scale for the present nanoindentation experiments. It should, however, be noted that the present model cannot account for the occurrence of multiple bursts and the kinetics of dislocation motion following their nucleation.

Similar calculations can also be made for other film thicknesses of polycrystalline Al. From Fig. 6, $h_b \approx 6$ nm and $\Delta h_b \approx 5$ nm for $t_f = 600$ nm, and $h_b \approx 10$ nm and $\Delta h_b \approx 14$ nm for $t_f = 1000$ nm. The above analysis yields $R_d \approx 18$ nm for $t_f = 600$ nm and $R_d \approx 26.5$ nm for $t_f = 1000$ nm. These predictions are also comparable to the contact radii at the onset of the first displacement burst. This result further implies that the contact area does not change in concurrence with the postulates of the model and with the expectation based on the consolidated elastic response.

5. CONCLUSIONS

On the basis of nanoindentation experiments conducted on single crystal and polycrystal Al thin films and polycrystal Cu thin films on Si substrates, and the accompanying TEM and AFM observations and analyses, the following conclusions are drawn.

1. Both single crystal and polycrystal thin films exhibit periodic displacement bursts at essentially constant loads during load-controlled nanoindentation.
2. The first displacement burst appears to occur when the maximum shear stress at the indenter tip is of the order of the theoretical shear strength of the material.
3. The nanoindentation response of the film in between the displacement bursts is found to be purely elastic and representative of the behavior under a "sharp" Berkovich indenter. At low loads or penetration depths, this elastic behavior, which is independent of film thickness but is

influenced by the crystallographic texture of the film, is characterized by Kick's law, equation (2): $P = C'h^2$, and can be predicted solely from knowledge of the elastic properties of the film and the indenter.

4. Transmission electron microscopy of indented polycrystalline Cu films clearly reveals the existence of a significantly higher density of dislocations (around the indentation) than in the as-deposited (unindented) film. The punching of arrays of dislocations within the grains surrounding the indentation is also evident in the TEM images. Atomic force microscopy of the indented Al films has confirmed the pile-up of material around the sharp Berkovich indentation.
5. It is postulated that the displacement bursts induced in the thin films by nanoindentation are primarily a consequence of the punching of geometrically necessary, prismatic dislocation loops. The accompanying rotation of the lattice is manifested as material pile-up around the indentation.
6. A simple energetics model is proposed in this paper to rationalize the accumulation of prismatic dislocation loops during the first displacement burst and to estimate the extent of the first displacement burst during nanoindentation. This model rests on the premise that the total elastic energy stored in the film at the onset of the first displacement burst fully accounts for the energies of interaction among the dislocation loops punched out during the displacement burst. The ensuing analytical predictions of the dislocation loop diameter are seen to be consistent with the indentation contact diameter induced at the appropriate loads for different film thicknesses.
7. An approximate measure of the overall plastic deformation and yield response of the thin film has also been extracted from the bounds of the nanoindentation load vs displacement plots comprising displacement bursts. This measure of the yield behavior of the thin film scales with the film thickness in that the resistance to overall microplasticity is greater at smaller film thicknesses. The resulting prediction of the yield strength as a function of film thickness for Al and Cu films is qualitatively in accord with the (yield strength vs film thickness) trends inferred from independent substrate curvature and X-ray diffraction measurements for a variety of f.c.c metal films.

Acknowledgements—This work was supported by the Office of Naval Research under Grant N-0014-94-1-0139 to MIT, and by the Advanced Materials Program of the Singapore-MIT Alliance. H.-J.K. is grateful to the Center for Advanced Aerospace Materials at POSTECH, S. Korea, for the award of a post-doctoral fellowship during his stay at the Laboratory for Experimental and Computational Micromechanics at MIT. Special thanks are extended to V.T. Srikar, S. Seel and C.V. Thompson

for generously providing the single crystal Al and polycrystal Cu films for the nanoindentation experiments conducted in this work. The authors are also grateful to T.-G. Nieh and B.W. Choi for help with some of the nanoindentation experiments reported in this paper. K.-Y.Z. and S.S. also acknowledge use of experimental facilities at the Royal Institute of Technology, Stockholm, and the Institute of Materials Research and Engineering at the National University of Singapore. K.J. Van Vliet, T.A. Venkatesh, E. Andrews and C.V. Thompson provided helpful comments on this manuscript.

REFERENCES

1. Oliver, W. C. and Pharr, G. M., *J. mater. Res.*, 1992, **7**, 1564.
2. Suresh, S. and Giannakopoulos, A. E., *Acta mater.*, 1998, **46**, 5755.
3. Giannakopoulos, A. E. and Suresh, S., *Scripta mater.*, 1999, **40**, 1191.
4. Bolshakov, A., Oliver, W. C. and Pharr, G. M., *J. mater. Res.*, 1997, **11**, 760.
5. Special Issue. *J. mater. Res.*, 1999, **14**.
6. Johnson, K. L., *Contact Mechanics*. Cambridge University Press, Cambridge, 1985.
7. Larsson, P.-L., Giannakopoulos, A. E., Soderlund, E., Rowcliffe, D. J. and Vestergaard, R., *Int. J. Solids Struct.*, 1996, **33**, 221.
8. Venkatesh, T. A., Van Vliet, K. J., Giannakopoulos, A. E. and Suresh, S., *Scripta mater.*, in press.
9. Tadmor, E. B., Miller, R., Phillips, R. and Ortiz, M., *J. mater. Res.*, 1999, **14**, 2233.
10. Corcoran, S. G., Colton, R. J., Lilleodden, E. T. and Gerberich, W. W., *Phys. Rev. B*, 1997, **55**, 16057.
11. Gerberich, W. W., Nelson, J. C., Lilleodden, E. T., Anderson, P. and Wyrobek, J. T., *Acta mater.*, 1996, **44**, 3585.
12. Wu, T. W., Hwang, C., Lo, J. and Alexopoulos, P. S., *Thin Solid Films*, 1988, **166**, 299.
13. Ljungcrantz, H., Oden, M., Holtman, L., Green, J. E. and Sundgren, J. E., *J. Appl. Phys.*, 1996, **80**, 6725.
14. Fivel, M. C., Robertson, C. F., Canova, G. R. and Boulanger, L., *Acta mater.*, 1998, **46**, 6183.
15. Page, T. F., Oliver, W. C. and McHargue, C. S., *J. mater. Res.*, 1992, **7**, 450.
16. Zielinski, W., Huang, H., Venkatraman, S. and Gerberich, W. W., *Phil. Mag. A*, 1995, **72**, 1221.
17. Tsui, T. Y. and Pharr, G. M., *J. mater. Res.*, 1999, **14**, 292.
18. Suresh, S., Nieh, T.-G. and Choi, B. W., *Scripta mater.*, 1999, **41**, 951.
19. Sawa, T., Akiyama, Y., Shimamoto, A. and Tanaka, K., *J. mater. Res.*, 1999, **14**, 2228.
20. Joo, Y. C., Electromigration failure and reliability of single-crystal and polycrystalline aluminium interconnects for integrated circuits. Ph.D. Dissertation, Massachusetts Institute of Technology 1995.
21. Lucas, B. N., Oliver, W. C. and Swindman, J. E., *Mat. Res. Soc. Symp. Proc.* ed. N.R. Moody, W.W. Gerberich, N. Burnham and S.P. Baker. Materials Research Society, Warrendale, PA, 1998, **522**, 3.
22. Vlassak, J. J. and Nix, W. D., *Phil. Mag. A*, 1993, **67**, 1045.
23. Vlassak, J. J. and Nix, W. D., *J. Mech. Phys. Sol.*, 1994, **42**, 1223.
24. Venkatraman, R., Bravman, J. C., Nix, W. D., Davies, P. W., Flinn, P. A. and Fraser, D. B., *J. Electronic mater.*, 1990, **10**, 1231.
25. Kobrinsky, M. and Thompson, C. V., *Acta mater.*, 2000, **48**, 625.
26. Chu, E., Shen, Y.-L. and Suresh, S., *Lexcom Report*. Massachusetts Institute of Technology, Cambridge, MA, 1996.
27. Keller, R.-M., Baker, S. P. and Arzt, E., *J. mater. Res.*, 1998, **13**, 1307.
28. Besser, P. R., X-ray determination of thermal strains and stresses in thin aluminium films and lines. Ph.D. Dissertation, Stanford University, 1993.
29. Flinn, P. A., *J. mater. Res.*, 1991, **6**, 1498.
30. Gouldstone, A., Choi, B.-W., Nieh, T.-G. and Suresh, S., Unpublished research 1999.
31. Marsh, D. M., *Proc. Royal Soc. London*, 1964, **A279**, 420.
32. Johnson, K. L., *J. Mech. Phys. Solids*, 1970, **18**, 115.
33. Smakula, A. and Klein, M. W., *J. Optical Soc. Am.*, 1949, **39**, 445.
34. Seitz, F., *Phys. Rev.*, 1950, **79**, 723.
35. Hill, R., Lee, E. H. and Tupper, S. J., *Proc. Royal Soc. London*, 1947, **A188**, 273.
36. Gane, N. and Cox, M., *Phil. Mag.*, 1971, **A48**, 881.
37. Brown, L. M., Khan, M. Y. and Chaudhri, M. M., *Phil. Mag.*, 1988, **A57**, 187.
38. Ma, Q. and Clarke, D. R., *J. mater. Res.*, 1995, **10**, 853.
39. Boldt, P. H., Weatherly, G. C. and Embury, J. D., A transmission electron microscope study of hardness indentations in MoSi₂, McMaster University Report, submitted.
40. Nabarro, F. R. N., *Adv. Phys.*, 1952, **1**, 269.
41. Hirth, J. P. and Lothe, J., *Theory of Dislocations*, 2nd ed. John Wiley, New York, 1982.